



Lateral Undrained Capacity of a Multiline Ring Anchor in Clay

Junho Lee, S.M.ASCE¹; and Charles P. Aubeny, Ph.D., P.E., F.ASCE²

Abstract: Offshore wind energy is an attractive alternative in pursuing the nation's clean energy goals due to the significant demand for electricity in the coastal areas of the United States. Locating sites further offshore in deeper water can provide stronger, more consistent wind power resources and can mitigate aesthetic concerns. This motivates a need for improvements in the floating offshore wind turbine (FOWT) technology. As foundation costs comprise a significant fraction of the total cost for offshore wind power development, reducing the cost of the mooring system can play a significant role in making floating offshore wind economically competitive. Previous studies led to the development of a novel, efficient multiline ring anchor (MRA) system that can provide significant capital cost savings. Preliminary research shows that the MRA has a clear advantage under lateral loading by attaching wing plates to the cylindrical core of the anchor. In this study, two-dimensional finite-element (2D FE) analyses were performed to understand how wing plates affect the MRA performance under horizontal loading and provide reliable estimates of the ultimate load capacity. The results show the collapse mechanisms and bearing factors can be affected by width, the total number of wing plates, and load angles. This study also presents plastic limit analysis (PLA), based on the upper bound solution, to validate the 2D FE results by comparison and to confirm whether the postulated collapse mechanism was correct. The results obtained in the current study indicated that PLA can be a benchmark solution to evaluate the ultimate load capacity of the MRA with a satisfactory agreement with the FE-computed values. DOI: 10.1061/(ASCE)GM.1943-5622.0001995.

Introduction

Offshore wind can play an important role in pursuing the clean energy goals of the United States, especially in coastal states where much of the energy demand is concentrated (Musial et al. 2016). Compared to land renewable energy resources, offshore wind is more consistent, has fewer aesthetic issues, and is close to population centers. A significant portion of potential offshore wind resources exists at water depths greater than 60 m, the depth beyond which floating systems are considered economically feasible. This leads to a need for cost-effective floating offshore wind turbine (FOWT) systems. The key to making FOWTs competitive is reducing the capital cost of its support system, of which moorings and anchors are a major component. The versatile and costeffective multiline ring anchor (MRA, Lee and Aubeny 2020) system has been developed with a view toward contributing to this cost reduction. The MRA consists of an embedded ring anchor with up to six mooring lines. Optional wing plates and keying flaps can be attached to improve load capacity (Fig. 1). Since the MRA combines the efficiency of the plate anchor with the availability of the multiline attaching the cylindrical anchor, it has relatively high geotechnical efficiency and fewer footprints compared to conventional caissons. A preliminary comparative study for anchors in soft clay (Lee and Aubeny 2020) shows that an MRA equipped with wing plates can achieve parity in lateral load capacity with a suction caisson of the same diameter and a length three times that of the MRA. Thus, wing plates can be an effective means for enhancing lateral load capacity as well as compensating for the shortened length of the MRA relative to conventional caissons. Moreover, fewer footprints and lighter anchors can reduce capital costs, including material, fabrication, transport, and installation costs (Lee et al. 2020). Other attractive features of the MRA include robust performance under unintentional loading, installability in a wide range of soils, and capability of precise positioning and deep embedment depth (Fig. 2).

Existing anchor alternatives for offshore floating wind include driven piles, suction caissons, drag embedded plate anchors, dynamically installed piles, suction embedded plate anchors, dynamically installed plate anchors, and pile-driven plate anchors. The relative merits of these alternatives are discussed by O'Loughlin et al. (2015), Diaz et al. (2016), Aubeny (2017), Li et al. (2017), Fontana et al. (2019), Lee and Aubeny (2020), and Huang and Han (2020). While any of these options may be advantageous under certain conditions, the various plate alternatives do not lend themselves easily to a multiline arrangement. In regard to the cylindrical anchors that can serve as multiline anchors, only driven piles can be deeply embedded into virtually any soil profile. The MRA can both accommodate multiple mooring lines and is also installable in essentially the same range of soil profiles as driven piles but is much smaller than a pile. Suction caissons are also amenable to a multiline configuration, but the range of soil conditions for which they are installable is more limited than piles. Further, aside from soft clay soil profiles, deep embedment by suction is not possible, limiting their vertical load capacity. By contrast, the MRA can provide vertical uplift resistance in virtually any soil profile.

While the vision of the MRA is to have a full range of capabilities in cohesive and granular soils for both horizontal and inclined loading, this study is a one thrust area in part of an overall study for evaluating MRA performance: horizontal load capacity in cohesive soil. With wing plates being a promising means for enhancing the effectiveness of the MRA, the particular focus of this study is to evaluate their effectiveness for various wing plate dimensions

¹Ph.D. Candidate, Zachry Dept. of Civil and Environmental Engineering, Texas A&M Univ., 199 Spence St., College Station, TX 77843 (corresponding author). ORCID: https://orcid.org/0000-0001-9644-3292. Email: juno918@tamu.edu

²Professor, Zachry Dept. of Civil and Environmental Engineering, Texas A&M Univ., 199 Spence St., College Station, TX 77843.

Note. This manuscript was submitted on June 11, 2020; approved on December 2, 2020; published online on February 23, 2021. Discussion period open until July 23, 2021; separate discussions must be submitted for individual papers. This paper is part of the *International Journal of Geomechanics*, © ASCE, ISSN 1532-3641.

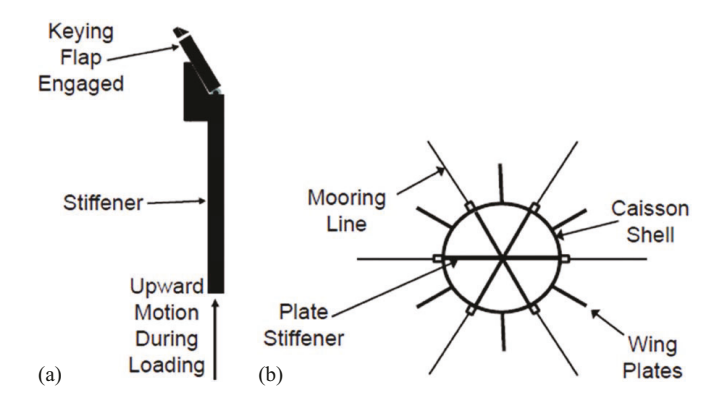


Fig. 1. Strategies for enhancing load capacity: (a) keying flaps; and (b) wing plates. (Reprinted with permission from Lee and Aubeny 2020.)

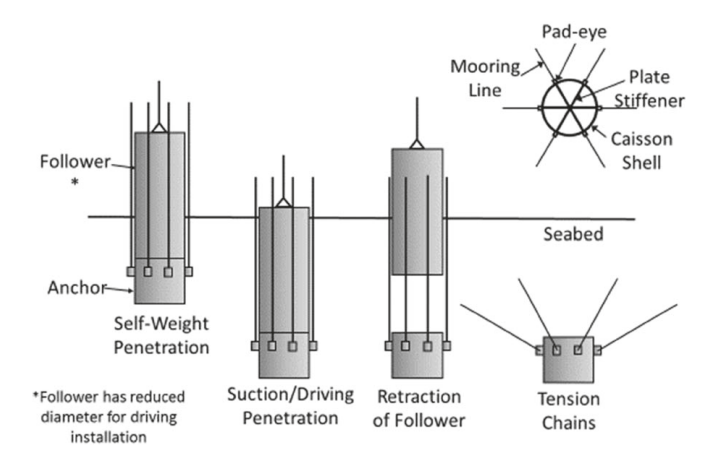


Fig. 2. Installation procedure of the MRA. (Reprinted with permission from Lee and Aubeny 2020.)

and configurations. The scope of the study presented herein is limited to pure horizontal loading approximated by a plane strain analysis of a translating anchor equipped with wing plates. The reason behind adopting this relatively simple model is that it permits the development of closed-form upper bound plastic limit analysis (PLA) solutions, which provide a useful tool for validating finite-element solutions. Noting the limited attention given to composite tubular-plate anchors to date, few reference solutions exist for validating the current studies. Accordingly, the PLA solutions provide an essential independent verification of the FE analyses. Parallel studies to this effort include three-dimensional FE analyses to evaluate the effects of a finite anchor length, moment loading, vertical loading, and inclined loading (Aubeny and Lee 2020).

As enhanced horizontal load capacity is key to an economical MRA in clay, this study investigates how wing plates alter both the collapse mechanism and undrained bearing capacity of the anchor. Lee and Aubeny (2019) conducted a limited two-dimensional finite-element (FE) study along these lines, but a more rigorous study is needed to fully understand the effects of (1) the size of the wing plates relative to the cylindrical core; (2) the number of wing plates; and (3) the direction of the resultant load. In regard to the last item, one should note that the addition of wing plates introduces a dependence of load direction on load capacity.

Under conditions of deep embedment and no volume change (undrained loading), FE analyses typically over-estimate the true collapse load. To overcome this tendency, various numerical analysis

approaches have been developed and applied, such as remeshing and interpolation technique by small stain (RITSS), efficient arbitrary Lagrangian-Eulerian (EALE), and coupled Eulerian-Lagrangian (CEL) (Benson 1989; Chen et al. 2013; de Sousa et al. 2011; Hu and Randolph 1998; Potts et al. 2001). However, these approaches still have commonly low computational efficiency and high complexity, resulting in a barrier to practicing engineers (Wang et al. 2015). For these reasons, where possible, it is desirable to complement FE analyses with lower and upper bound PLA solutions that can bracket the exact solution (Aubeny 2017). Useful contributions relevant to this study can be found in the works of Randolph and Houlsby (1984), Murff and Hamilton (1993), Aubeny et al. (2001, 2003), O'Neill et al. (2003), Rowe and Davis (1982), Merifield et al. (2001), Yang et al. (2010), and Yu et al. (2011). While they provide a useful starting point for the current study, these studies are limited to simple strip or circular shapes. By contrast, the MRA wing plates involve more complex failure mechanisms that depend on load angle, the total number of wing plates, and the width of wing plates.

In view of the aforementioned discussion, the present study adopts the following approach. Finite-element studies are first conducted to establish how the wing plates affect the failure mechanism of the anchor. Based on these insights, upper bound PLA solutions are developed to provide analytical solutions for the anchor bearing resistance. These, in turn, are compared to the FE estimates of bearing resistance. While neither solution is exact, a reasonable agreement between PLA and FE can provide some measure of improved confidence in the solutions. Additionally, for the limiting cases of vanishingly small and infinitely large wing plates, exact solutions exist (simple cylinder and simple plate, respectively). Comparing limiting case FE and PLA solutions to such exact solutions provides a further means for obtaining improved confidence in the results of the analyses presented herein.

Finite-Element Analyses

The commercial software ABAQUS version 2018 (SIMULIA 2018) was used to conduct the 2D, plane strain analyses described below. All analyses were carried out under displacement-controlled conditions to investigate the ultimate load capacity of the MRA. Displacement-controlled analyses have the advantage that numerical problems do not occur as loading approaches the limit state. Analyses were for pure horizontal translation, corresponding to the case of the load attachment depth at its optimal position. All analyses presumed undrained loading conditions, which are typical of wave loading on a floating structure moored to an anchor embedded in a clay seabed. This assumption was valid so long as a nondimensional rate of loading ($V = vd/c_v$, where V = nondimensional velocity, v = rate of penetration, d = diameter of the penetrometer, and $c_v =$ coefficienct of consolidation) exceeded 30 (Chung et al. 2006).

Soil Model

The FE model assumes linearly elastic-perfectly behavior below a Tresca yield surface and associated flow at yield. A Poisson's ratio $\mu=0.49$ approximates undrained loading. As the anchor is assumed to be deeply embedded and no gapping occurs, the FE-computed values are not affected by soil weight and the soil can be assumed to be weightless. Full bonding was assumed at the soil–anchor interface. Murff et al. (2005) showed that the adhesion factor had a slight effect on the ultimate capacity of plate anchor oriented normally to the loading direction. A series of the FE analyses in the present study yielded results consistent with this trend, with the change in a bearing factor

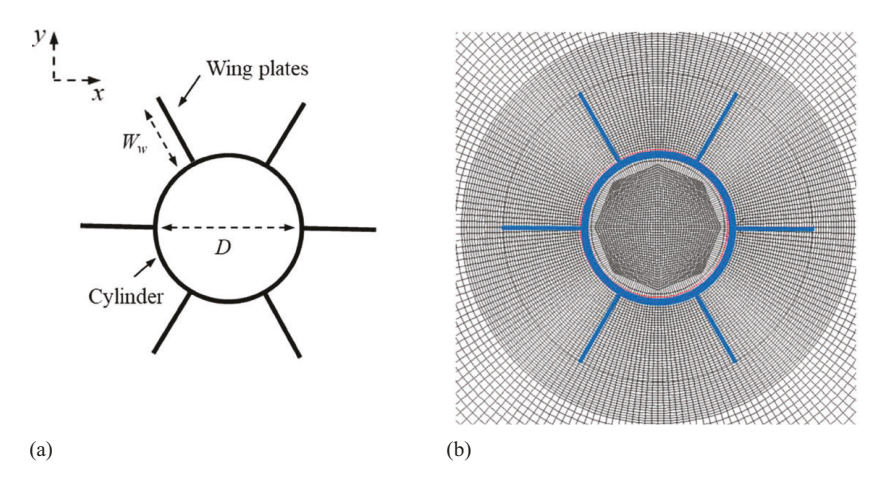


Fig. 3. Dimensions and 2D FE mesh: (a) dimensions of the MRA; and (b) 2D FE mesh

over a range of adhesion $\alpha = 0.1-1.0$ never exceeding 4%. Given the insensitivity of computed bearing factors to changes in α , a fully rough bonding at the soil–anchor interface, $\alpha = 1$, was assumed in the parametric studies. Since the focus of this study was on ultimate load capacity, and since the elastic behavior does not influence the ultimate load capacity (Chen 1975), stress–strain behavior was assumed as linear with Young's modulus $E/s_u = 800$.

Dimensions and Discretization

The dimensions of the MRA are defined in Fig. 3, a 1-m-diameter caisson with wing plate widths varying 0.12-1.5 m. The soil was modeled using first-order, fully integrated elements (four-node element, CPE4), with the boundary was placed 15 equivalent diameter $15D_{\rm eq}$ away from the MRA. The far-field was modeled using four-node one-way infinite elements (CINPE4). The caisson and wing plates were assumed as a rigid body. A typical FE mesh consisted of around 32,000 elements. Element dimensions varied from about 1/200 of the MRA circumference near the anchor–soil interface to between 0.04 and 0.4 m in regions far from the MRA.

Validation

The case of no wing plates corresponded to that of a translating cylinder, for which Randolph and Houlsby (1984) provided an exact solution. They showed that for the fully rough and smooth cases, which were $\alpha = 1$ and 0.1, the lateral bearing factors were 11.94 and 9.53, respectively. The FE simulation for this case (Fig. 4) gave lateral bearing factors $N_{pp} = 12.16$ ($\alpha = 1$) and $N_{pp} = 9.68$ ($\alpha = 0.1$), slightly overpredicting the exact solution by about 1.8% and 1.6%, respectively. Considering two- and four-wing anchors with wing plate widths exceeding the cylinder radius, $W_w \ge R$, and loading normal to the wing plates, Fig. 5(a) shows a collapse mechanism essentially identical to a simple plate. The FE-computed bearing factor for these cases was $N_{pp} = 11.51$, about 0.8% greater than the exact solution for a plate $N_{pp} = 11.42$, calculated by using Aubeny (2017). Therefore, comparing the FE solutions to the limiting circular and plate solutions, for which exact solutions were available, indicated satisfactory accuracy for the FE solutions, i.e., within 2%.

Plastic Limit Analysis

Plastic limit analysis (PLA) deals with statically admissible (lower bound) and kinematically admissible (upper bound), which do not

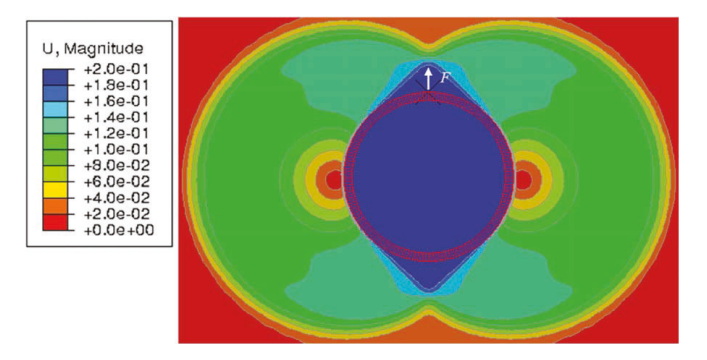


Fig. 4. Cylinder with no wing plates.

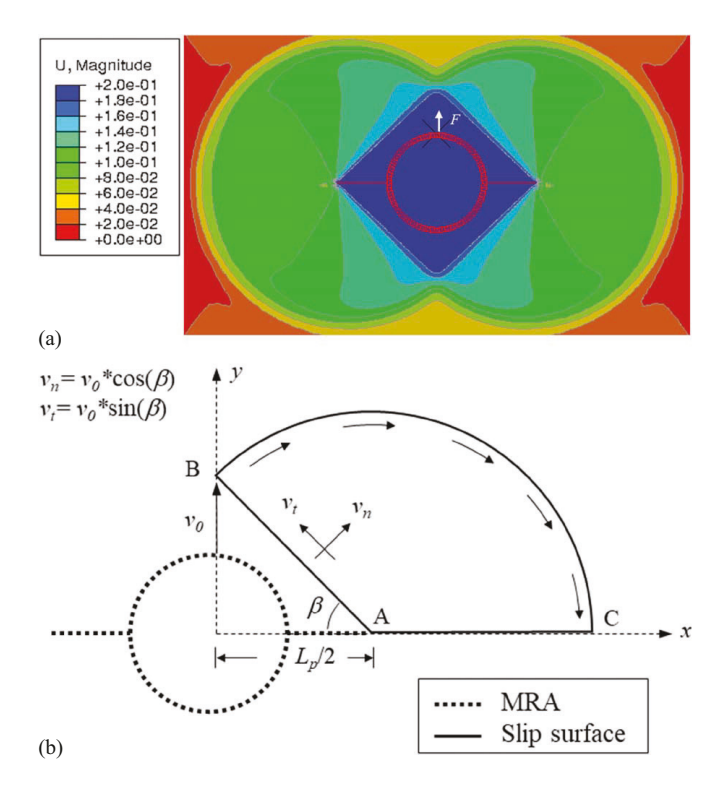


Fig. 5. Two-wing anchor loaded at $\theta_a = 0^\circ$: (a) 2D FE failure mechanism; and (b) postulated failure mechanism for upper bound.

violate the yield criterion of the soil mass. Upper bound solutions were computed by virtual work analysis of a postulated kinematically admissible collapse mechanism, while lower bound solutions required statically admissible stress fields such as those provided using the method of characteristics (Aubeny 2017). Since the upper bound solution was relatively more straightforward and computationally effective for routine design, the following parts of this study will focus on developing upper bound solutions considering complex geometric configurations.

Different definitions were possible for the anchor lateral bearing factor $N_p = F/s_u L$, where F = collapse load; $s_u = \text{soil undrained}$ shear strength; and L = selected characteristic dimension of the anchor. Bang et al. (2003) took $L = L_p$, where $L_p =$ projected length of the cylinder-wing plate system normal to the direction of the applied load. The bearing factor computed in this manner was denoted as $N_{pp} = F/s_u L_p$ in this paper. An alternative definition of the bearing factor is $N_{pc} = F/s_uD$, where D = diameter of the cylindrical core section of the anchor. The former definition has the advantage of direct comparison to existing solutions for cylinders and plates, while the latter has the advantage of providing a clear picture of how the wing plates enhance load capacity. This paper used both definitions according to the topic of interest. The projected area could vary depending on the width and number of wing plates and the load angle of the MRA. This study defined the load angle θ_a to be zero when it was normal to the line segment defining the maximum projected length L_p of the anchor, which corresponded to the direction of a line that bisects the arc between any two wing plates. By this definition, θ_{amax} occurred at half the angular spacing between the wing plates, or 90°, 60°, 45° and 30° from the nearest wing plate for $N_w = 2, 3, 4$, and 6, respectively or, in general, $\theta_{a\text{max}} = 180^{\circ}/N_w$.

The projected width L_p of the MRA with wing plates is a function of the number of wing plates N_w , the wing plate width W_w , and the load angle θ_a . For an even number of wing plates, $N_w = 2$, 4, and 6, L_p may be expressed as follows:

$$L_p = 2 \times \max \left\{ R, \ \left| (R + W_w) \sin \left(\frac{\pi}{2} - \theta_a \right) \right| \right\}$$
 (1)

For $N_w = 3$, the projected length becomes

$$L_{p} = \max \left\{ R, \ \left| (R + W_{w}) \sin \left(\frac{\pi}{N_{w}} - \theta_{a} \right) \right| \right\}$$

$$+ \max \left\{ R, \ \left| (R + W_{w}) \sin \left(\frac{\pi}{N_{w}} + \theta_{a} \right) \right| \right\}$$
(2)

When $W_w \ge R$, a simpler alternative to Eq. (1) is

$$L_p = 2(R + W_w)\cos\theta_a \tag{3}$$

Likewise, when $W_w \ge R$ Eq. (2) for $N_w = 3$ can be substituted with the following simpler expression:

$$L_p = 2(R + W_w) \cos\left(\frac{\pi}{2N_w}\right) \cos\theta_a \tag{4}$$

An upper bound PLA postulates a kinematically admissible collapse mechanism, computing the virtual rates of internal energy dissipation and external virtual work, and equating the two to obtain a collapse load. This approach may optimize the geometry of the failure mechanism to seek a least upper bound PLA solution (Aubeny 2017). This study uses the FE displacement fields at incipient collapse as a guide to developing realistic collapse mechanisms

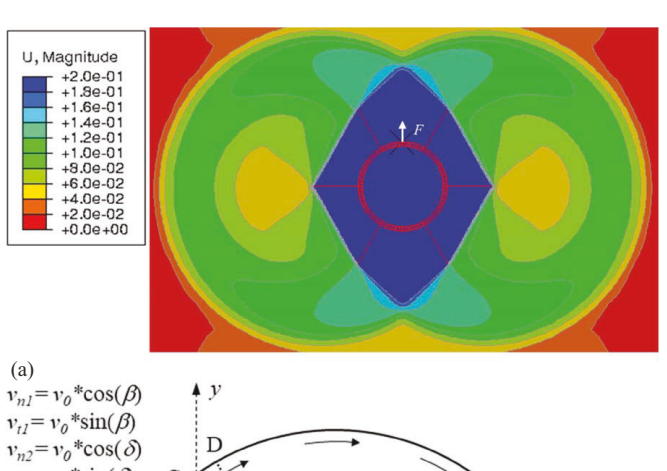
(Figs. 5–10). Except one load case for the three-wing anchor, symmetry allows PLA calculations to proceed solely on the basis of the upper right quadrant of the collapse mechanisms discussed in the following. All PLA solutions apply to an MRA with the wing plate width equal to the radius of the core cylinder, $W_w = R$. Due to its dependence on the number of wing plates and load angle, the bearing factor will be denoted as a function of the two parameters considered in the PLA study, N_{pp} (N_w , θ_a).

Six-Wing Anchor Loaded at $\theta_a = 0$

Lee and Aubeny (2019) showed that failure mechanisms for two-wing and four-wing anchors approach that of a strip anchor when the wing plates exceed the cylindrical core radius, $W_w \ge R$, and the direction of applied loading is $\theta_a = 0^{\circ}$ [Fig. 5(a)]. By contrast, the existence of six-wings distributed at equal intervals around the circumference of the cylinder produces an elongation of the simple strip anchor failure mechanism [Fig. 6(a)], although the projected area still equals that of the two-wing or four-wing cases. The FE-computed bearing factor for this case is $N_{pp}(6, 0^{\circ}) = 11.74$, slightly exceeding the bearing factor for a two- or four-wing anchor, $N_{pp}(2, 0^{\circ}) = 11.51$. To provide a basis for validating the FE prediction, a PLA solution can be developed for the postulated collapse mechanism shown in Fig. 6(b). This mechanism comprises a rigid core section (OABC) and three circular sections (BCD, BDEF, and ABF). Internal energy dissipation occurs at five slip surfaces (AB, BC, CD, DE, and BF) and within three continuously deforming regions (ABF, BCD, and BDEF).

The rate of energy dissipation along with slip surface AB is

$$\dot{D}_{AB} = s_u v_0 L_p \left(\frac{\tan \delta}{2} \right) (1 - \sin \theta) \tag{5}$$



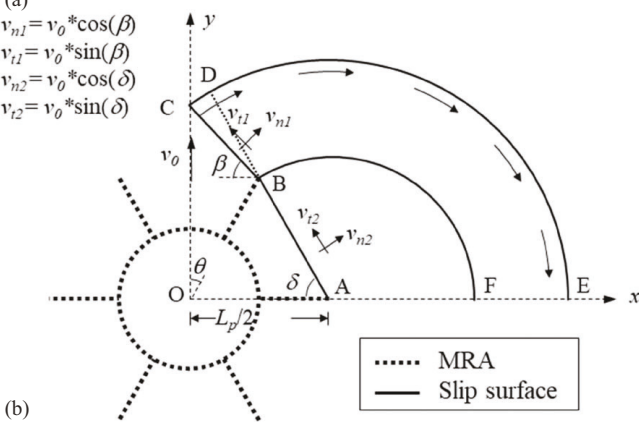


Fig. 6. Six-wing anchor with $\theta_a = 0^\circ$: (a) 2D FE failure mechanism; and (b) postulated failure mechanism for upper bound.

where s_u = undrained shear strength; v_0 = upward velocity; and L_p = 2D = projected length of the anchor. Triangle OAB in Fig. 6(b) is equilateral, requiring δ = 60° and θ = 30°. Triangle OBC is defined by the angle β , which is an optimization variable that, through trial and error, seeks a least upper bound solution (Fig. 11).

For surface BC

$$\dot{D}_{\rm BC} = s_u v_0 L_p \left(\frac{\tan \beta}{2}\right) \sin \theta \tag{6}$$

For surface CD

$$\dot{D}_{\rm CD} = s_u v_0 L_p \left(\frac{\sin \theta}{2} \right) (\delta - \beta) \tag{7}$$

For surface DE

$$\dot{D}_{\rm DE} = s_u v_0 L_p \left\{ \left(\frac{\cos \delta}{\cos \beta} \frac{\sin \theta}{2} + \frac{1 - \sin \theta}{2} \right) (\pi - \delta) \right\}$$
 (8)

For surface BF

$$\dot{D}_{\rm BF} = s_u v_0 L_p \left(\frac{1 - \sin \theta}{2} \right) (\pi - \delta) \tag{9}$$

For internal deforming region ABF

$$\dot{D}_{ABF} = s_u v_0 L_p \left(\frac{1 - \sin \theta}{2} \right) (\pi - \delta) \tag{10}$$

For internal deforming region BCD

$$\dot{D}_{\rm BCD} = s_u v_0 L_p \left(\frac{\sin \theta}{2} \right) (\delta - \beta) \tag{11}$$

For internal deforming region BDEF

$$\dot{D}_{\text{BDEF}} = s_u v_0 L_p \left(\frac{\cos \delta}{\cos \beta} \frac{\sin \theta}{2} \right) (\pi - \delta)$$
 (12)

Equating the rate of external work Fv_0 to the sum of the energy dissipation terms leads to the following expression for bearing factor of the lateral resistance of the MRA, N_{pp} :

$$N_{pp}(6, \ 0^{\circ}) = \frac{F}{s_{u}L_{p}} = 4\left[\left(\frac{\tan\delta}{2}\right)(1-\sin\theta) + \left(\frac{\tan\beta}{2}\right)\sin\theta + \sin\theta(\delta-\beta) + (\pi-\delta)\left\{\frac{3}{2}(1-\sin\theta) + \frac{\cos\delta}{\cos\beta}\sin\theta\right\}\right]$$
(13)

Following O'Neill et al. (2003) and Aubeny (2017), the solution presented previously is formulated in terms of a triangular wedge angle β that can be optimized to obtain a least upper bound. A choice of an optimal $\beta = 20.7^{\circ}$ (Fig. 11) Eq. (13) yields a bearing factor N_{pp} (6, 0°) = 12.00, which exceeds the FE prediction by about 2.2%.

Four-Wing and Six-Wing Anchors Loaded at θ_{amax}

Since these load orientations do not induce rotation, symmetrical collapse mechanisms such as those depicted in Figs. 7(a) and 8(a) develop. Figs. 7(b) and 8(b) present postulated PLA mechanisms for these cases. They comprise one rigid wedge (OAB), one shear fan zone (ABC), and one rigid block (ACDE). Taking advantage of symmetry, five dissipation functions can fully evaluate the internal energy dissipation. Selecting the upper right quadrant as the basis for analysis, the mechanism comprises the slip interfaces, AB, BC, AE, and CD, and internal deforming region ABC. Due to the similarity in their collapse mechanisms, the four-wing and six-wing cases may be considered together, the difference between these cases being embodied in the θ angle, where $\theta_a = 45^{\circ}$ for the four-wing case and $\theta = 60^{\circ}$ for the six-wing case.

The rate of energy dissipation along surface AB is

$$\dot{D}_{AB} = s_u \nu_0 L_p \left(\frac{\tan \beta}{2} \right) \tag{14}$$

where s_u = undrained shear strength; v_0 = upward velocity; L_p = unit length of the projected area; and β = angle of the triangular wedge. For surface BC

$$\dot{D}_{\rm BC} = s_u \nu_0 L_p \left(\frac{\pi - \beta}{2} \right) \tag{15}$$

For surface AE

$$\dot{D}_{AE} = s_u v_0 L_p \left(\frac{1 + \cos \beta}{2 \tan \theta} \right) \tag{16}$$

where θ = angle between the applied load and the closest wing plate.

For surface CD

$$\dot{D}_{\rm CD} = s_u v_0 L_p \left(\frac{\cos \beta}{2 \tan \theta} \right) \tag{17}$$

For internal deforming region ABC

$$\dot{D}_{ABC} = s_u v_0 L_p \left(\frac{\pi - \beta}{2} \right) \tag{18}$$

Equating the rate of external work Fv_0 to the sum of the energy dissipation terms leads to the following expression for bearing factor N_{pp} is:

$$N_{pp} = \frac{F}{s_u L_p} = 4 \left[(\pi - \beta) + \left(\frac{\tan \beta}{2} \right) + \frac{1 + 2\cos \beta}{2\tan \theta} \right]$$
 (19)

For the four-wing case, the angle θ becomes 45° and the optimal β is 58.9°, producing a PLA bearing factor N_{pp} (4, 45°) = 15.84 (Fig. 11). The FE bearing factor for this case is 14.92; thus, the PLA upper bound solution exceeds the FE solution by 5.8%.

For the six-wing case, the angle θ becomes 60° and the optimal β is 54.4°, producing a PLA bearing factor N_{pp} (6, 30°) = 14.06 (Fig. 11). The FE bearing factor for this case is 13.46; thus, the PLA upper bound solution exceeds the FE solution by 4.3%.

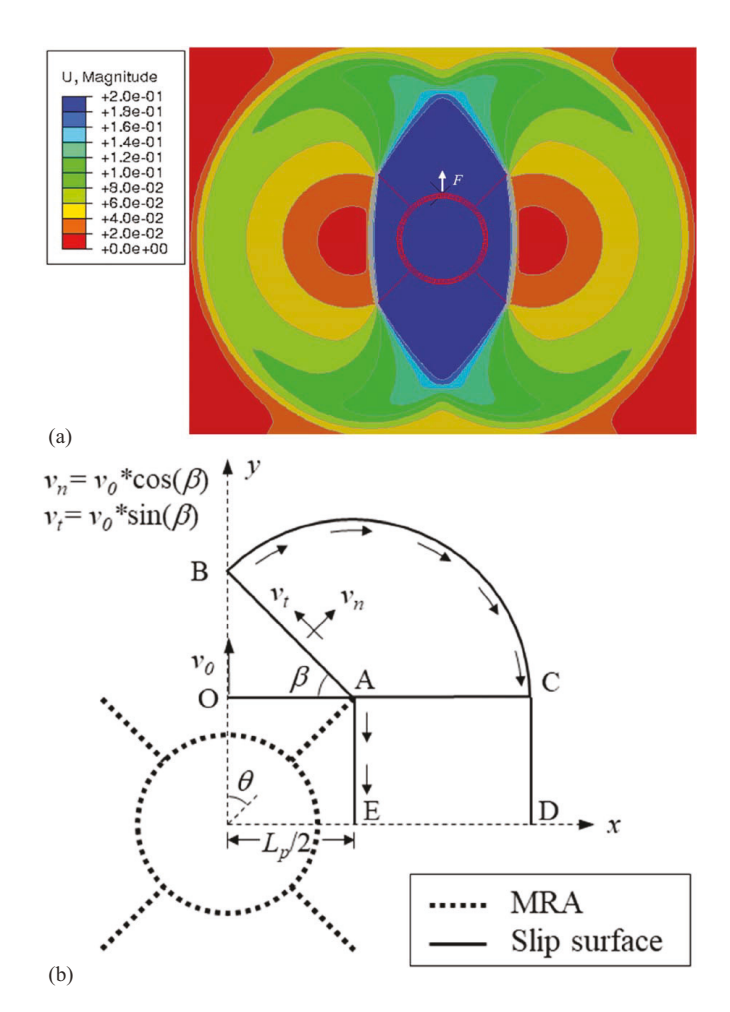


Fig. 7. Four-wing anchor loaded at $\theta_a = 45^\circ$: (a) 2D FE failure mechanism; and (b) postulated failure mechanism for upper bound.

Three-Wing Anchor Loaded at $\theta_a = 30^{\circ}$ and 0°

Unlike the purely translational failure mechanisms discussed until this point, the collapse mechanism for six-wing anchor loaded at $\theta_a = 30^{\circ}$ comprises both rotational and translational motions. Based on the displacement fields in Fig. 9(a), Fig. 9(b) shows the postulated failure mechanism, which includes linear slip surfaces (AO, BO, and AB), circular slip surface (ACB), and circular shear zone (AOB). The rates of energy dissipation functions are derived as follows:

For surfaces AO and BO

$$\dot{D}_{AO} = \dot{D}_{BO} = s_u v_0 L_p \tan \beta \tag{20}$$

For surface AB

$$\dot{D}_{AB} = s_u v_0 L_p \left(\frac{1}{\cos \beta}\right) \tag{21}$$

For surface ACB

$$\dot{D}_{\text{ACB}} = s_u v_0 L_p 2(\pi - \beta) \tag{22}$$

For internal deforming region AOB

$$\dot{D}_{AOB} = s_u v_0 L_p 2(\pi - \beta) \tag{23}$$

Equating the rate of external work Fv_0 to the sum of the energy dissipation terms leads to the following expression for bearing

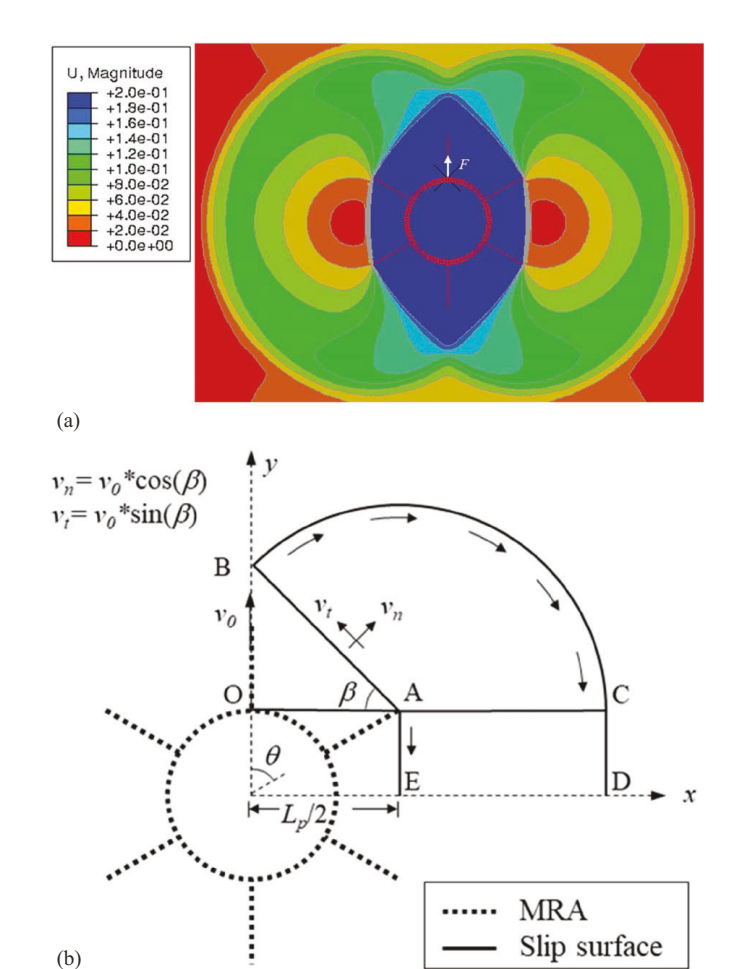


Fig. 8. Six-wing anchor with $\theta_a = 30^\circ$: (a) 2D FE failure mechanism; and (b) postulated failure mechanism for upper bound.

factor of the lateral resistance of the MRA, N_{pp} :

$$N_{pp}(3,30^{\circ}) = \frac{F}{s_u L_p} = \left[2 \tan \beta + \frac{1}{\cos \beta} + 4(\pi - \beta) \right]$$
 (24)

The optimal β -angle in this case turns out to be simply the minimum physically permissible angle $\beta = 30^{\circ}$, for which the PLA bearing factor becomes N_{pp} (3, 30°) = 12.78. The FE predicted bearing factor is 12.80, so the two solutions match within 0.2%.

Fig. 10(b) presents postulated PLA mechanism for a three-wing MRA with $\theta_a = 0^\circ$ case. The collapse mechanism has a rigid zone (BAFE), a rigid block (ACDF), and two shear fans (ABC and DEF) having the same radius, thereby providing a kinematically admissible mechanism. The triangular wedges ABC and DEF have defined angle β , an optimization variable that seeks a least upper bound solution through trial and error. Taking advantage of symmetry, five dissipation functions can fully evaluate the internal energy dissipation. Selecting the right-side bisect as the basis for analysis, the mechanism comprises the slip interfaces, AB, BC, CD, DE, EF, and AF, and internal deforming regions ABC and DEF.

The rate of energy dissipation along surfaces AB and EF is

$$\dot{D}_{AB} = \dot{D}_{EF} = s_u v_0 L_p \left(\frac{\tan \beta}{2} \right)$$
 (25)

where s_u = undrained shear strength; v_0 = upward velocity; L_p = unit length of the projected area; and β = angle of the triangular wedge.

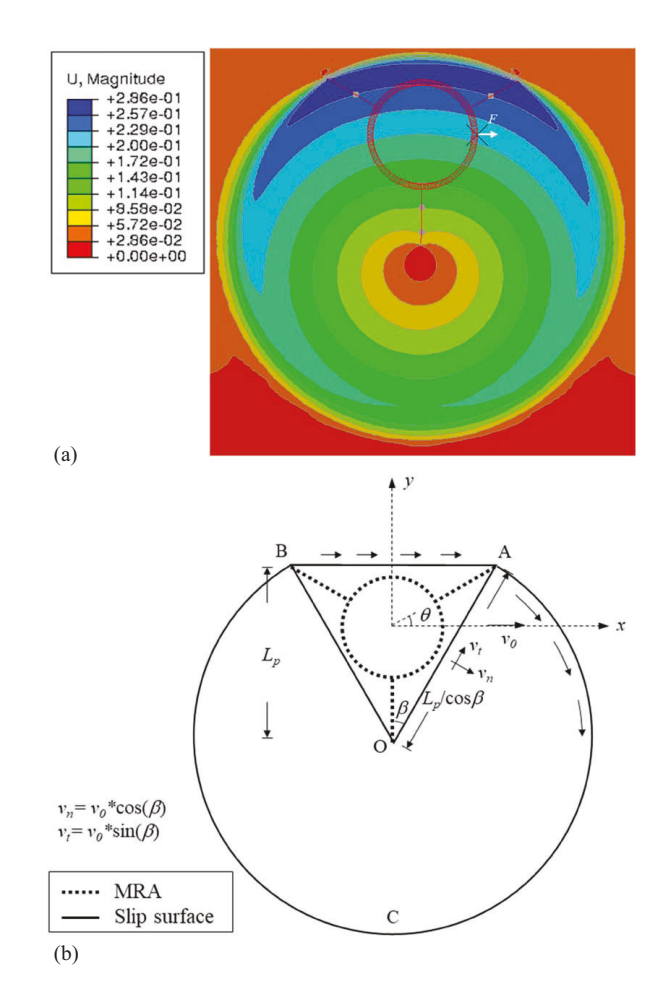


Fig. 9. Three-wing anchor loaded at $\theta_a = 30^\circ$: (a) 2D FE failure mechanism; and (b) postulated failure mechanism for upper bound.

For surfaces BC and DE

$$\dot{D}_{\rm BC} = \dot{D}_{\rm DE} = s_u v_0 L_p \left(\frac{\pi - \beta}{2}\right) \tag{26}$$

For surface AF

$$\dot{D}_{\rm AF} = s_u v_0 L_p \left(\frac{1 + \cos \beta}{2} \right) \left(\frac{\cos \theta + 1}{\sin \theta} - \tan \beta \right) \tag{27}$$

For surface CD

$$\dot{D}_{\rm CD} = s_u \nu_0 L_p \left(\frac{\cos \beta}{2} \right) \left(\frac{\cos \theta + 1}{\sin \theta} - \tan \beta \right) \tag{28}$$

For internal deforming regions ABC and DEF

$$\dot{D}_{ABC} = \dot{D}_{DEF} = s_u v_0 L_p \left(\frac{\pi - \beta}{2} \right)$$
 (29)

Equating the rate of external work Fv_0 to the sum of the energy dissipation terms leads to the following expression for bearing factor N_{pp} is:

$$N_{pp}(3,0^{\circ}) = \frac{F}{s_u L_p}$$

$$= 2\left[2(\pi - \beta) + \tan\beta + \left(\frac{1}{2} + \cos\beta\right) \left(\frac{\cos\theta + 1}{\sin\theta} - \tan\beta\right)\right] (30)$$

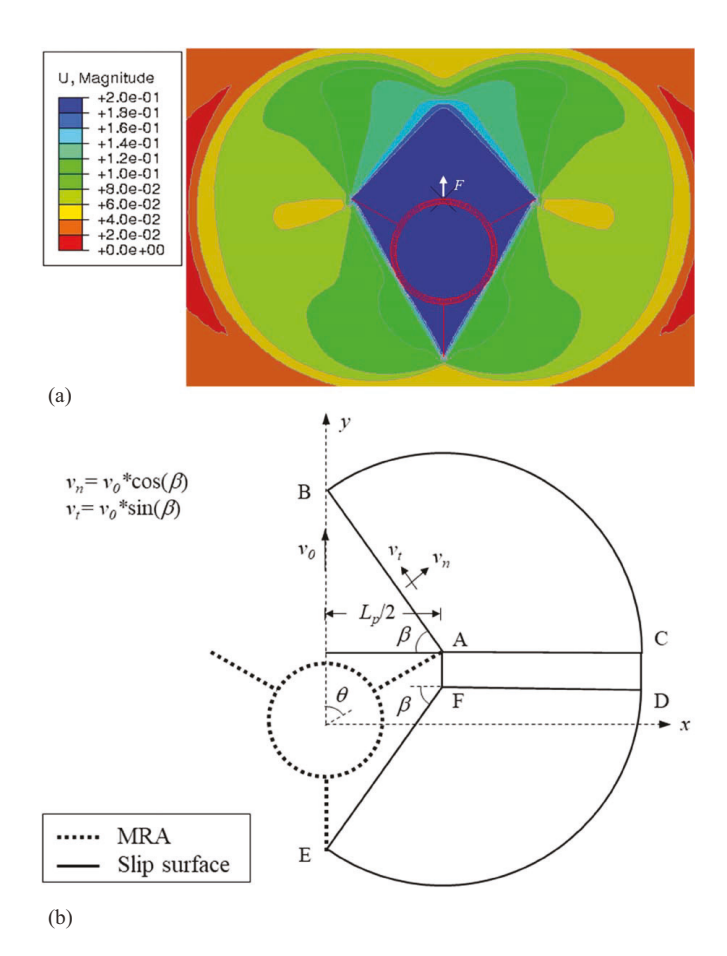


Fig. 10. Three-wing anchor with $\theta_a = 0^\circ$: (a) 2D FE failure mechanism; and (b) postulated failure mechanism for upper bound.

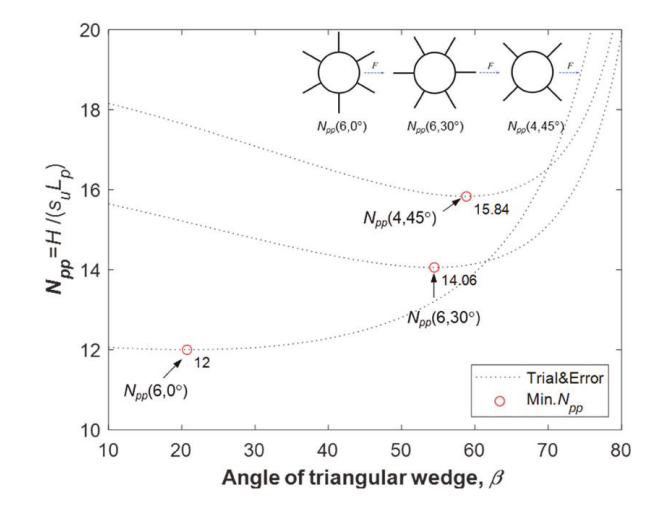


Fig. 11. Trial and error curve for optimizing the triangular wedge angle β .

The optimal β -angle, in this case, turns out to be simply the minimum physically permissible angle $\beta = 60^{\circ}$, for which the PLA bearing factor becomes N_{pp} (3, 0°) = 11.84. The FE predicted bearing factor is 11.83, so the two solutions match within 0.1%.

Summary

Table 1 summarizes FE predictions of N_{pp} for various numbers of wing plates N_w and load angles θ_a . Agreement between PLA and FE is generally within 5% and always within 6%.

Table 1. FE and PLA values for lateral bearing factor

			N_{pp}		FE – PLA		
$N_w (W_w = R)$	$ heta_a$	Postulated failure	FE	PLA	$\frac{PL-PLA}{PLA}$ (%)	Ref. Eqn.	Ref. Fig.
No wing	0°	TR	12.16	11.94	+1.8	<u>—</u>	Fig. 4
2	0°	TR	11.53	11.45	+0.7		Fig. 5
3	0° 30°	TR w/SRB TR-TORS	11.83 12.80	11.84 12.78	-0.1 +0.2	(30) (24)	Fig. 10 Fig. 9
4	0° 45°	TR TR w/RSB	11.54 14.92	11.45 15.84	+0.8 -5.8	— (19)	Fig. 5 Fig. 7
6	0° 30°	TR TR w/RSB	11.78 13.46	12.00 14.06	-2.2 -4.3	(13) (19)	Fig. 6 Fig. 8

Note: TR = translational movement; TR-TORS = combined behaviors with translational and torsional; and TR w/SRB = translational movement having a rigid side block

Parametric Study

Description

To understand how wing plates alter the failure mechanism and lateral bearing factor, this study evaluated the following parameters (Fig. 12):

- width of the wing plates, W_w ;
- number of wing plates around the ring anchor, N_w ;
- angle between the applied load and the plane of wing plates, θ_a;
 and
- adhesion factor between pile and soil, α

In these analyses, the parametric study considered a 1-m-diameter cylinder with two-wings, three-wings, four-wings, and six-wings. Each width of wing plates varies from 0.12 m (R/4) to 1.5 m (3R). The FE study considered the effect of the load angle θ_a , varying from 0° to the maximum θ_a for each case.

In comparing the effect of wing width W_w on anchor capacity, it is useful to compare cases having the same maximum projected width L_p . For this reason, the anchor wing plate configuration and load cases were sub-divided into the two groups shown in Fig. 13 and Table 2. Group I comprises anchors where the number of wing plates N_w is some multiple of 2 loaded $\theta_a = 0$. Group II includes anchors with N_w being some multiple of 3 that are loaded at angles θ_a that produce the same L_p .

Effect of Width of Wing Plates

As the width of wing plates increases, illustrated in Figs. 14 and 15, the lateral resistance H of the MRA increases. To a large extent, this is a direct consequence of the increase in the projected width L_p . For example, in the case of Group I, as the projected width L_p of the anchor increases from $L_p = 2D$ ($W_w/R = 1$) to $L_p = 4D$ ($W_w/R = 3$), N_{pc} nearly doubles (Fig. 14). Likewise, the same trend has been shown in Group II (Fig. 15). In all cases, N_{pc} increases nearly linearly with increasing W_w . Figs. 16 and 17 present the same results in terms of N_{pp} . In these figures, the bearing factors show a general trend of transitioning from a simple cylinder to a simple plate solution. Due to the similarity of the predicted MRA bearing factors (N_{pp}) to plate solutions, comparison to experimental studies of bearing factors for vertical strip plate anchors is instructive. Experimental data by Ranjan and Arora (1980) and Chen et al. (2015) show bearing factors

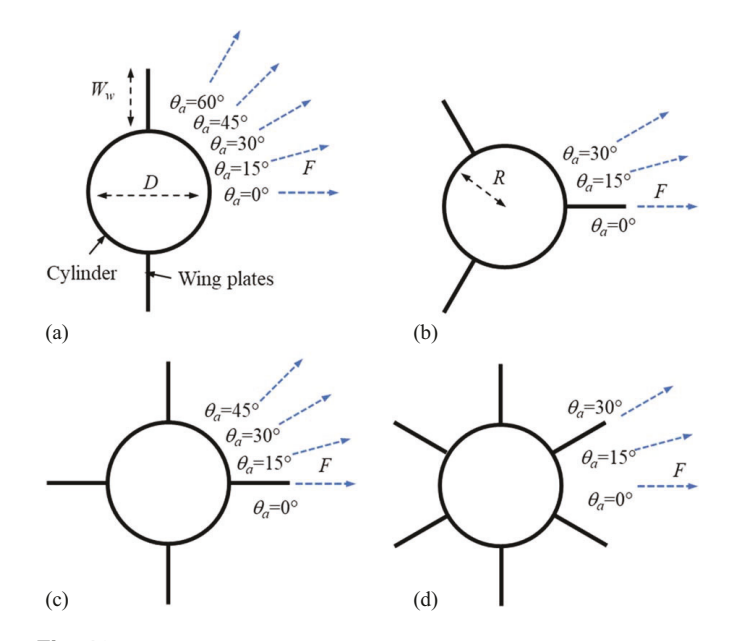


Fig. 12. Cross-section view of the MRA including W_w , N_w , and θ_a : (a) two-wings; (b) three-wings; (c) four-wings; and (d) six-wings.

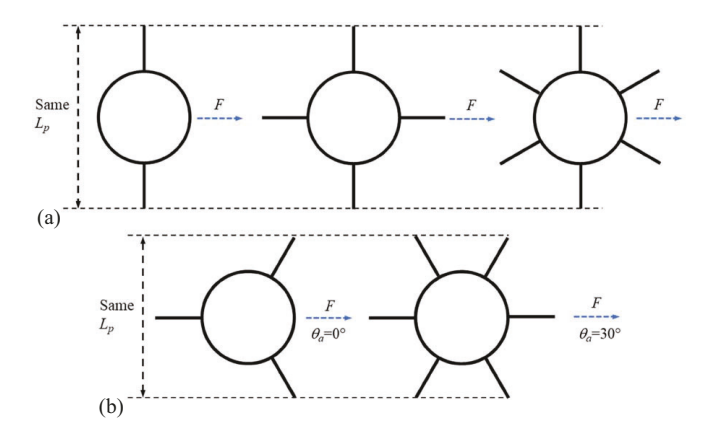


Fig. 13. Comparing group for each parameter: (a) Group I; and (b) Group II.

Table 2. Comparing group for each parameter

Comparing		Parameters			
group	Description	W_w	N_w	θ_a	
I	Anchors with $N_w = 2$, 4, and 6 loaded $\theta_a = 0$ [Fig. 13(a)]	Figs. 14 and 16	Figs. 14 and 16	Fig. 18	
II	Anchors with $N_w = 3$ and 6 loaded at angles θ_a that produce the same L_p [Fig. 13(b)]	Figs. 15 and 17	Figs. 15 and 17	_	

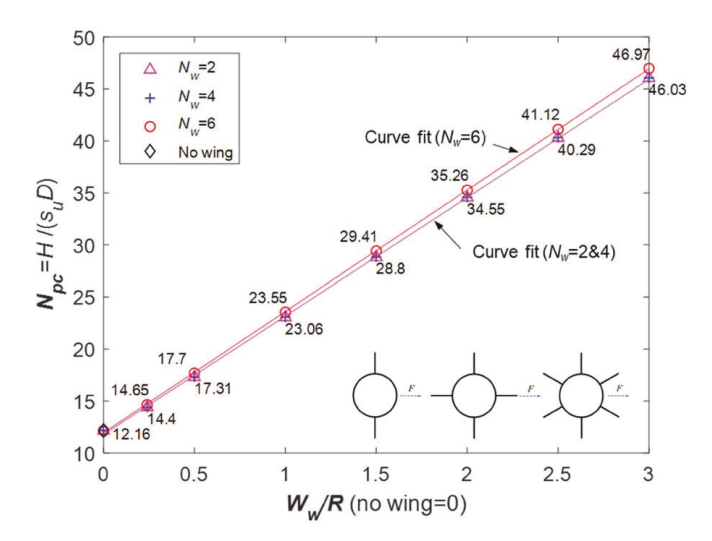


Fig. 14. Effect of W_w and N_w on Group I anchors.

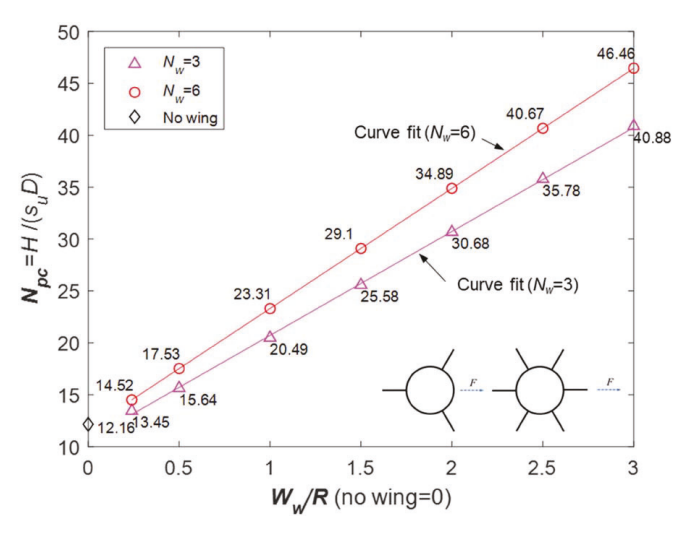


Fig. 15. Effect of W_w and N_w on Group II anchors.

varying from 11 to 11.5, that is, within 2.6% of the MRA bearing factors computed in this study. The exception is the Group II case for a six-wing anchor, which shows a nearly uniform value of N_{pp} for all wing widths that is somewhat higher (about 12%) than the exact solution for a cylinder.

Effect of the Number of Wing Plates

In the case of Group I, as shown in Fig. 14, the lateral resistance *H* for four-wings is as same as that of two-wings, even though it

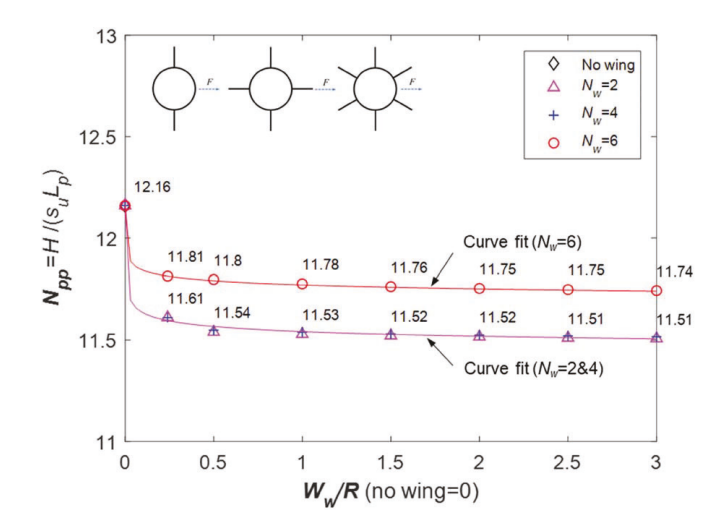


Fig. 16. Bearing factor on two-wing, four-wing, and six-wing MRA.

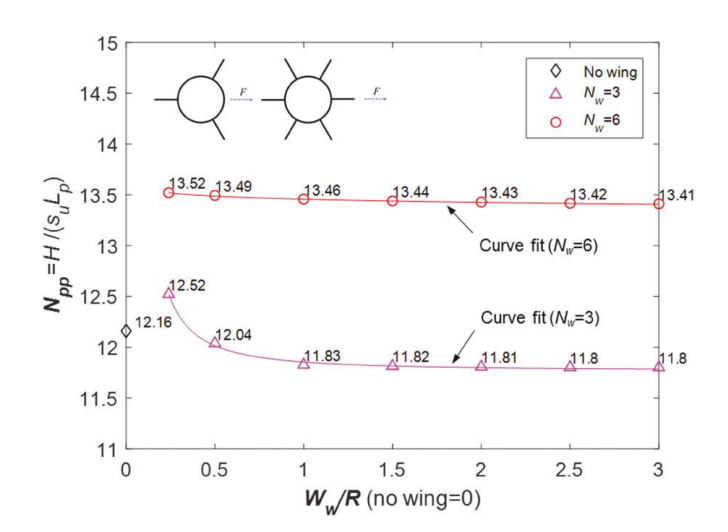


Fig. 17. Bearing factor on three-wing and six-wing MRA.

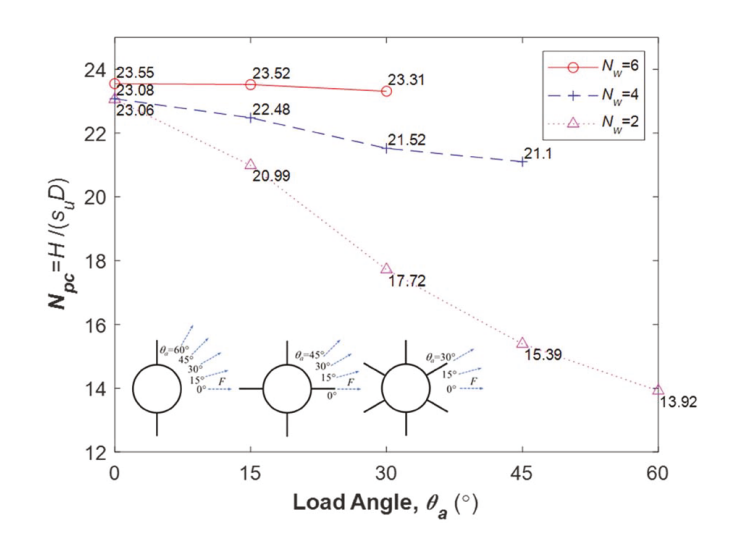


Fig. 18. Effect of θ_a on two-wing, four-wing, and six-wing MRA.

has two additional wing plates since the additional wing plates are within the yielded region that would occur without these plates. On the other hand, the addition of two more wings to create a two-wing anchor slightly increases H, by about 2%. A similar but more pronounced trend occurs in the case of Group II (Fig. 15). Thus, in addition to the predictable result that N_{pc} increases with increasing L_p , the wing plates can alter the collapse mechanism. Figs. 8 and 10 indicate the failure mechanism to the extent that there is significant sensitivity to the number of wing plates N_w .

Effect of Load Angle

To elucidate the effects of load angle, two-wing, four-wing, and six-wing cases were considered. Since the projected area was maximum when the load angle was zero, increases in load angle θ_a to its

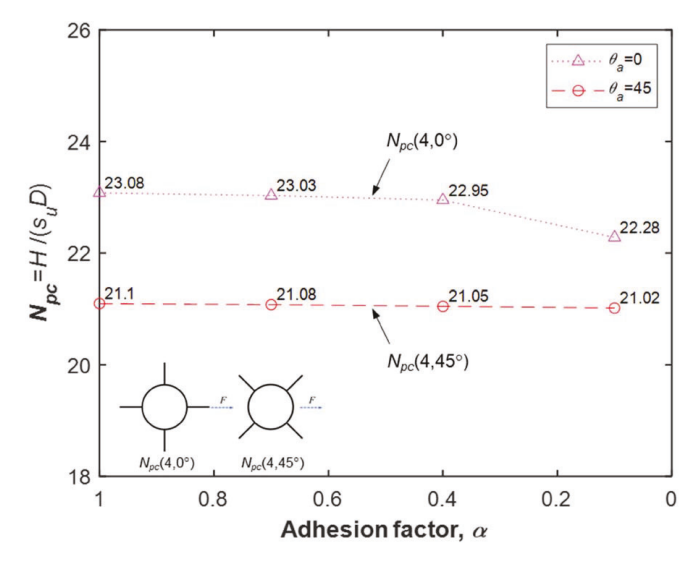


Fig. 19. Effect of α on four-wing MRA.

maximum value were expected to decrease N_{pc} . Fig. 18 clearly shows this to be the case. In the two-wing case, the decrease in resistance with increasing load angle was most severe. However, only a minor reduction in N_{pc} occured with increasing θ_a for the case of a six-wing anchor. This suggested that, although the six-wing anchor provides only a modest increase in load resistance under favorable ($\theta_a = 0$) loading conditions, it is a much more reliable anchor under unfavorable loading conditions.

Effect of Adhesion Factor

As shown in Fig. 19, the adhesion factor has a slight or little to no effect on the lateral resistance of an MRA with wings. The parametric study considered a range of adhesion factors that vary from 0.1 to 1.0 for a four-wing anchor for load angles of 0° and 45° . A clear picture of little to no effect of adhesion factor was observed for $\theta_a = 45^{\circ}$. A possible explanation for this trend was related to the nature of the collapse mechanism, comprising rigid wedges and blocks, with a very small surface area of slippage between soil and the anchor [Fig. 7(a)]. For $\theta_a = 0^{\circ}$, up to 3.5% reduction of N_{pc} was observed with decreasing adhesion factors. Slippage at the tip of the wing plates may affect this reduction.

Curve Fit Equations

Table 3 shows curve fit equations to describe the sensitivity of MRA load capacity to variations in wing width increases as W_w increases. As noted previously, since the collapse load was independent of the elastic response of the soil (Chen 1975), the MRA bearing factors presented herein were valid, irrespective of the elastic behavior of the soil. Current thinking at this stage is that a wing plate width equal to the core cylinder radius, $W_w = R$, is most practical. The equations in Table 3 and Figs. 14 and 15 indicated that this wing plate dimension can nearly double the MRA load capacity. These equations and Fig. 18 show a six-wing anchor to be the least susceptible to reduction in load capacity under unfavorable load angle conditions.

Table 3. Equations of curve fit

Relationship	Group and N_w		Equations	R^2	Ref. Fig.
N_{pc} - W_w/R	I	2	$N_{pc} = 11.38 \left(\frac{W_w}{R}\right) + 11.79$	0.99	Fig. 14
		4	$N_{pc} = 11.4 \left(\frac{W_w}{R}\right) + 11.79$	0.99	
		6		0.99	
	II	3	$N_{pc} = 11.66 \left(\frac{W_w}{R}\right) + 11.95$ (W_w)	0.99	Fig. 15
		6	$N_{pc} = 10.01 \left(\frac{W_w}{R}\right) + 10.71$	1.00	<i>G</i>
		Ü	$N_{pc} = 11.59 \left(\frac{W_w}{R} \right) + 11.74$	0.00	
N_{pp} - W_w/R	I	2	$N_{pp} = 0.26 \left(\frac{W_w}{R}\right)^{-0.13} + 11.28$	0.99	Fig. 16
		4	$N_{pp} = 0.22 \left(\frac{W_w}{R}\right)^{-0.14} + 11.32$	0.99	
		6	$N_{pp} = 0.36 \left(\frac{W_w}{R}\right)^{-0.08} + 11.41$	0.99	
	II	3	\ /	0.99	Fig. 17
			$N_{pp} = 0.09 \left(\frac{W_w}{R}\right)^{-1.5} + 11.77$	0.99	G
		6	$N_{pp} = -1.57 \left(\frac{W_w}{R}\right)^{0.03} + 15.03$		

Concluding Remarks

This study presents the potential advantages of a novel, integrated, and networked multiline ring anchor system. Then, two-dimensional FE analyses are conducted to estimate the effect of the wing plates of the MRA in soft clay. Basic conclusions are as follows:

- Load capacity H increases nearly linearly with increasing wing width W_w (Figs. 14 and 15).
- Under the most favorable load angle condition, θ_a = 0, increasing the number of wing plates N_w only modestly increases load capacity H (Figs. 14 and 15).
- Four-wing and, especially, six-wing anchors are much less susceptible to reductions in load capacity under less favorable load angles, i.e., $\theta_a > 0$ (Fig. 18).

Appendix. Plastic Limit Solutions

Six-Wing Anchor Loaded at $\theta_a = 0$

The upward velocity assumes as v_0 during the upward translation of the wedge OABC [Fig. 6(b)]. The normal and tangential components of velocity for surfaces AB and BC can be denoted as the function of the angles β and δ , $v_{n1} = v_0 \cos \beta$, $v_{t1} = v_0 \sin \beta$, $v_{n2} = v_0 \cos \delta$, and $v_{t2} = v_0 \sin \delta$, respectively. The magnitude of the velocity along with arcs BF and DE should equal to v_{n1} and v_{n2} , respectively.

The rate of energy dissipation along with slip surface AB is

$$\dot{D}_{AB} = s_u v_{t2} \overline{AB} = s_u v_{t2} \frac{L_p (1 - \sin \theta)/2}{\cos \delta} = s_u v_0 L_p \left(\frac{\tan \delta}{2}\right) (1 - \sin \theta)$$
(31)

where s_u = undrained shear strength; v_0 = upward velocity; and $L_p = 2D$ = projected length of the anchor. Triangle OAB in Fig. 6(b) is equilateral, requiring $\delta = 60^\circ$ and $\theta = 30^\circ$. Triangle OBC is defined by the angle β , which is an optimization variable that, through trial and error, seeks a least upper bound solution.

For surface BC

$$\dot{D}_{\rm BC} = s_u v_{t1} \overline{\rm BC} = s_u v_{t1} \frac{L_p \sin \theta / 2}{\cos \beta} = s_u v_0 L_p \left(\frac{\tan \beta}{2}\right) \sin \theta \qquad (32)$$

For surface CD

$$\dot{D}_{\text{CD}} = s_u v_{n1} \overline{\text{BC}}(\delta - \beta) = s_u v_{n1} \frac{L_p \sin \theta / 2}{\cos \beta} (\delta - \beta)$$

$$= s_u v_0 L_p \left(\frac{\sin \theta}{2}\right) (\delta - \beta)$$
(33)

For surface DE

$$\dot{D}_{DE} = s_u v_{n2} \overline{AD}(\pi - \delta)$$

$$= s_u v_{n2} \left\{ \frac{L_p (1 - \sin \theta)/2}{\cos \delta} + \frac{L_p \sin \theta/2}{\cos \beta} \right\} (\pi - \delta)$$

$$= s_u v_0 L_p \left\{ \left(\frac{\cos \delta}{\cos \beta} \frac{\sin \theta}{2} + \frac{1 - \sin \theta}{2} \right) (\pi - \delta) \right\}$$
(34)

For surface BF

$$\dot{D}_{\rm BF} = s_u v_{n2} \overline{\rm AB}(\pi - \delta) = s_u v_{n2} \frac{L_p (1 - \sin \theta)/2}{\cos \delta} (\pi - \delta)$$
$$= s_u v_0 L_p \left(\frac{1 - \sin \theta}{2}\right) (\pi - \delta) \tag{35}$$

Internal deforming region ABF can be considered as the shear fan in a polar coordinate $(r - \theta)$ system. While the circumferential component of the velocity v_{θ} equal to $v_0 \cos \delta$ at all points, the radial component v_r is zero everywhere. Considering these conditions, the single nonzero strain rate can be defined as a function of the angle of the wedge (Malvern 1969; Aubeny 2017):

$$\dot{\gamma}_{r\theta} = 2\dot{\varepsilon}_{r\theta} = 2\frac{1}{2} \left(\frac{1}{r} \frac{\partial v_r}{\partial \theta} + \frac{\partial v_{\theta}}{\partial r} - \frac{v_{\theta}}{r} \right) = -\frac{v_0 \cos \delta}{r}$$
 (36)

For internal deforming region ABF

$$\dot{D}_{ABF} = \int s_u |\dot{\gamma}|_{max} dV = \int_{\delta}^{\pi} \int_{0}^{L_p(1-\sin\theta)/2/\cos\delta} s_u \frac{v_0 \cos\delta}{r} r dr d\theta$$
$$= s_u v_0 L_p \left(\frac{1-\sin\theta}{2}\right) (\pi - \delta)$$
(37)

For internal deforming region BCD

$$\begin{split} \dot{D}_{\rm BCD} &= \int s_u |\dot{\gamma}|_{\rm max} dV = \int_{\beta}^{\delta} \int_{0}^{L_p \sin \theta/2/\cos \beta} s_u \frac{v_0 \cos \beta}{r} r dr d\theta \\ &= s_u v_0 L_p \left(\frac{\sin \theta}{2}\right) (\delta - \beta) \end{split} \tag{38}$$

For internal deforming region BDEF

$$\dot{D}_{\text{BDEF}} = \int s_u |\dot{\gamma}|_{\text{max}} dV = \int_{\delta}^{\pi} \int_{0}^{L_p \sin \theta / 2 / \cos \beta} s_u \frac{v_0 \cos \delta}{r} r dr d\theta$$
$$= s_u v_0 L_p \left(\frac{\cos \delta}{\cos \beta} \frac{\sin \theta}{2}\right) (\pi - \delta) \tag{39}$$

Equating the rate of external work Fv_0 to the sum of the energy dissipation terms leads to the following expression for bearing factor of the lateral resistance of the MRA, N_{pp} :

$$N_{pp}(6,0^{\circ}) = \frac{F}{s_u L_p} = 4 \left[\left(\frac{\tan \delta}{2} \right) (1 - \sin \theta) + \left(\frac{\tan \beta}{2} \right) \sin \theta + \sin \theta (\delta - \beta) + (\pi - \delta) \left\{ \frac{3}{2} (1 - \sin \theta) + \frac{\cos \delta}{\cos \beta} \sin \theta \right\} \right]$$
(40)

Four-Wing and Six-Wing Anchors Loaded at θ_{amax}

The upward velocity assumes as v_0 during the upward translation of the wedge OAB [Figs. 7(b) and 8(b)]. The normal and tangential

components of velocity for surface AB can be defined as the function of the angles β , $v_n = v_0 \cos \beta$, and $v_t = v_0 \sin \beta$, respectively. The magnitude of the velocity along with arc BC should equal to v_n .

The rate of energy dissipation along surface AB is

$$\dot{D}_{AB} = s_u v_t \overline{AB} = s_u v_t \frac{L_p/2}{\cos \beta} = s_u v_0 L_p \left(\frac{\tan \beta}{2}\right)$$
(41)

where s_u = undrained shear strength; v_0 = upward velocity; L_p = unit length of the projected area; and β = angle of the triangular wedge. For surface BC

$$\dot{D}_{\rm BC} = s_u v_n \overline{\rm BC} = s_u v_n \frac{L_p/2}{\cos \beta} (\pi - \beta) = s_u v_0 L_p \left(\frac{\pi - \beta}{2}\right) \tag{42}$$

For surface AE

$$\dot{D}_{AE} = s_u(v_0 + v_n)\overline{AE} = s_u(v_0 + v_n)\frac{L_p/2}{\tan \theta}$$

$$= s_u v_0 L_p \left(\frac{1 + \cos \beta}{2 \tan \theta}\right)$$
(43)

where θ = angle between the applied load and the closest wing

For surface CD

$$\dot{D}_{\rm CD} = s_u v_n \overline{\rm CD} = s_u v_n \frac{L_p/2}{\tan \theta} = s_u v_0 L_p \left(\frac{\cos \beta}{2 \tan \theta} \right)$$
 (44)

For internal deforming region ABC

$$\dot{D}_{ABC} = \int s_u |\dot{\gamma}|_{\max} dV = \int_{\beta}^{\pi} \int_{0}^{L_p/2/\cos\beta} s_u \frac{v_0 \cos\beta}{r} r dr d\theta$$
$$= s_u v_0 L_p \left(\frac{\pi - \beta}{2}\right) \tag{45}$$

Equating the rate of external work Fv_0 to the sum of the energy dissipation terms leads to the following expression for bearing factor N_{pp} is:

$$N_{pp} = \frac{F}{s_u L_p} = 4\left[(\pi - \beta) + \left(\frac{\tan \beta}{2}\right) + \frac{1 + 2\cos \beta}{2\tan \theta} \right]$$
 (46)

Three-Wing Anchor Loaded at $\theta_a = 30^\circ$

The rightward velocity assumes as v_0 during the rotational movement of the wedge OAB [Fig. 9(b)]. The normal and tangential components of velocity for surface AO can be defined as the function of the angles β , $v_n = v_0 \cos \beta$, and $v_t = v_0 \sin \beta$, respectively. The magnitude of the velocity along with circular slip surface ACB should equal to v_n .

For surfaces AO and BO

$$\dot{D}_{AO} = \dot{D}_{BO} = s_u v_t \overline{AO} = s_u v_0 \sin \beta \frac{L_p}{\cos \beta} = s_u v_0 L_p \tan \beta \qquad (47)$$

For surface AB

$$\dot{D}_{AB} = s_u v_0 \overline{AB} = s_u v_0 L_p \left(\frac{1}{\cos \beta}\right) \tag{48}$$

For surface ACB

$$\dot{D}_{ACB} = s_u v_n \overline{ACB} = s_u v_0 \cos \beta \left(\frac{L_p}{\cos \beta}\right) 2(\pi - \beta)$$

$$= s_u v_0 L_p 2(\pi - \beta) \tag{49}$$

For internal deforming region AOB

$$\dot{D}_{AOB} = \int s_u |\dot{\gamma}|_{max} dV$$

$$= \int_{\beta}^{2\pi-\beta} \int_{0}^{L_p/\cos\beta} s_u \frac{v_0 \cos\beta}{r} r dr d\theta = s_u v_0 L_p 2(\pi - \beta)$$
 (50)

Equating the rate of external work Fv_0 to the sum of the energy dissipation terms leads to the following expression for bearing factor of the lateral resistance of the MRA, N_{pp} :

$$N_{pp}(3, 30^{\circ}) = \frac{F}{s_u L_p} = \left[2 \tan \beta + \frac{1}{\cos \beta} + 4(\pi - \beta) \right]$$
 (51)

Three-Wing Anchor Loaded at $\theta_a = 0^\circ$

As shown in Fig. 10(b), the rate of energy dissipation along with surfaces AB and EF is

$$\dot{D}_{AB} = \dot{D}_{EF} = s_u v_t \overline{AB} = s_u v_t \frac{L_p/2}{\cos \beta} = s_u v_0 L_p \left(\frac{\tan \beta}{2}\right)$$
 (52)

where s_u = undrained shear strength; v_0 = upward velocity; L_p = unit length of the projected area; and β = angle of the triangular wedge.

For surfaces BC and DE

$$\dot{D}_{\rm BC} = \dot{D}_{\rm DE} = s_u v_n \overline{\rm BC} = s_u v_n \frac{L_p/2}{\cos \beta} (\pi - \beta) = s_u v_0 L_p \left(\frac{\pi - \beta}{2}\right)$$
 (53)

$$\dot{D}_{AF} = s_u(v_0 + v_n)\overline{AF} = s_u(v_0 + v_n)\frac{L_p}{2}\left(\frac{\cos\theta + 1}{\sin\theta} - \tan\beta\right)$$
$$= s_u v_0 L_p \left(\frac{1 + \cos\beta}{2}\right) \left(\frac{\cos\theta + 1}{\sin\theta} - \tan\beta\right)$$
(54)

For surface CD

$$\dot{D}_{\text{CD}} = s_u v_n \overline{\text{CD}} = s_u v_n \frac{L_p}{2} \left(\frac{\cos \theta + 1}{\sin \theta} - \tan \beta \right)$$
$$= s_u v_0 L_p \left(\frac{\cos \beta}{2} \right) \left(\frac{\cos \theta + 1}{\sin \theta} - \tan \beta \right) \tag{55}$$

For internal deforming region ABC and DEF

$$\dot{D}_{ABC} = \dot{D}_{DEF} = \int s_u |\dot{\gamma}|_{max} dV$$

$$= \int_{\beta}^{\pi} \int_{0}^{L_p/2/\cos\beta} s_u \frac{v_0 \cos\beta}{r} r dr d\theta = s_u v_0 L_p \left(\frac{\pi - \beta}{2}\right)$$
 (56)

Equating the rate of external work Fv_0 to the sum of the energy dissipation terms leads to the following expression for bearing factor N_{pp} is:

$$N_{pp}(3, 0^{\circ}) = \frac{F}{s_u L_p}$$

$$= 2\left[2(\pi - \beta) + \tan \beta + \left(\frac{1}{2} + \cos \beta\right) \left(\frac{\cos \theta + 1}{\sin \theta} - \tan \beta\right)\right] (57)$$

Data Availability Statement

All data, models, and codes generated or used during the study appear in the published article.

Acknowledgments

The authors acknowledge the support for the second author from the National Science Foundation, award number CMMI-1936901, and the Texas A&M High Performance Research Computing facility for the use of their resources in running the numerous finite-element analyses supporting this study.

Notation

The following symbols are used in this paper:

 A_p = projected area of the MRA;

 \hat{D} = diameter of the cylinder part of the MRA;

 \dot{D} = rate of energy dissipation;

E =Young's modulus;

F = applied load;

H = lateral resistance of the MRA per unit length;

L = characteristic width of MRA;

 L_p = projected width of MRA normal to load direction;

 N_p = dimensionless unit lateral bearing factor;

 $N_{pc} = H/(s_u D)$, lateral bearing factor based on D;

 $N_{pp} = H/(s_u L_p)$, lateral bearing factor based on L_p ;

 N_w = number of wing plates;

 s_u = undrained shear strength;

 v_0 = velocity of the anchor in the loading direction;

 $v_n = v_0 \cos \beta$, $v_0 \cos \delta$;

 $v_t = v_0 \sin \beta$, $v_0 \sin \delta$;

 W_w = width of the wing plates;

 α = adhesion factor between pile and soil;

 β , δ = angle of the triangular wedge;

 θ = angle between applied load and the closest wing; and

 θ_a = load angle from bisector between two wing plates.

References

Aubeny, C. 2017. Geomechanics of marine anchors. Boca Raton, FL: CRC Press.

Aubeny, C., J. Murf, and S. Moon. 2001. "Lateral undrained resistance of suction caisson anchors." *Int. J. Offshore Polar Eng.* 11 (3): 211–219.

Aubeny, C. P., S. W. Han, and J. D. Murff. 2003. "Inclined load capacity of suction caissons." *Int. J. Numer. Anal. Methods Geomech.* 27 (14): 1235–1254. https://doi.org/10.1002/nag.319.

Aubeny, C. P., and J. Lee. 2020. "Horizontal load capacity of multiline ring anchor in soft clay." In *Int. Symp. on Frontiers in Offshore Geotechnics*. Austin, TX: Deep Foundations Institute.

Bang, S., Y. Cho, Y. Kim, D. Kwag, and T. Lee. 2003. "Embedded suction anchors for floating breakwaters." WIT Trans. Built. Environ. 70: 469–477.

Benson, D. J. 1989. "An efficient, accurate, simple ale method for nonlinear finite element programs." Comput. Methods Appl. Mech. Eng. 72 (3): 305–350. https://doi.org/10.1016/0045-7825(89) 90003-0.

Chen, J., C. F. Leung, Z. Chen, K. K. Tho, and Y. K. Chow. 2015. Centrifuge model study on pullout behavior of plate anchors in clay with linearly increasing strength, 839–844. Leiden, Netherlands: Taylor & Francis Books.

Chen, W.-F. 1975. *Limit analysis and soil plasticity*. Amsterdam, Netherlands: Elsevier.

Chen, Z., K. K. Tho, C. F. Leung, and Y. K. Chow. 2013. "Influence of overburden pressure and soil rigidity on uplift behavior of square plate anchor in uniform clay." *Comput. Geotech.* 52: 71–81. https:// doi.org/10.1016/j.compgeo.2013.04.002.

Chung, S. F., M. F. Randolph, and J. A. Schneider. 2006. "Effect of penetration rate on penetrometer resistance in clay." *J. Geotech. Geoenviron. Eng.* 132 (9): 1188–1196. https://doi.org/10.1061/(ASCE)1090-0241(2006) 132:9(1188).

de Sousa, J. R. M., C. S. de Aguiar, G. B. Ellwanger, E. C. Porto, D. Foppa, and C. J. de Medeiros. 2011. "Undrained load capacity of torpedo anchors embedded in cohesive soils." *J. Offshore Mech. Arct. Eng.* 133 (2): 021102. https://doi.org/10.1115/1.4001953.

Diaz, B. D., M. Rasulo, C. P. Aubeny, C. M. Fontana, S. R. Arwade, D. J. DeGroot, and M. Landon. 2016. "Multiline anchors for floating offshore wind towers." In OCEANS 2016 MTS/IEEE Monterey, 1–9. New York: IEEE.

Fontana, C., S. Arwade, D. DeGroot, S. Hallowell, C. Aubeny, B. Diaz, M. Landon, S. Ozmutlu, and A. Myers. 2019. "Force dynamics and stationkeeping costs for multiline anchor systems in floating wind farms with different spatial parameters." In *Proc.*, 38th Int. Conf. on Ocean, Offshore and Arctic Engineering, 1–11. New York: ASME.

Hu, Y., and M. Randolph. 1998. "A practical numerical approach for large deformation problems in soil." *Int. J. Numer. Anal. Methods Geomech.* 22 (5): 327–350. https://doi.org/10.1002/(SICI)1096-9853(199805) 22:5<327::AID-NAG920>3.0.CO;2-X.

Huang, Y., and X. Han. 2020. "Features of earthquake-induced seabed liquefaction and mitigation strategies of novel marine structures." J. Mar. Sci. Eng. 8 (5): 310. https://doi.org/10.3390 /jmse8050310.

Lee, J., and C. P. Aubeny. 2019. "Effect of wing plates on a multiline ring anchor system in cohesive soils." In OCEANS 2019 MTS/IEEE SEATTLE, 1–6. New York: IEEE. https://doi.org/10.23919 /OCEANS40490.2019.8962734.

Lee, J., and C. P. Aubeny. 2020. "Multiline ring anchor system for floating offshore wind turbines." J. Phys.: Conf. Series 1452 (1): 012036.

Lee, J., M. Khan, L. Bello, and L. P., Aubeny. 2020. "Cost analysis of multiline ring anchor systems for offshore wind farm." *Deep Foundation Institute 45th Conf.*, 484–493. National Harbor, MD: Deep Foundations Institute.

Li, H., H. Liu, and S. Liu. 2017. "Dynamic analysis of umbrella suction anchor foundation embedded in seabed for offshore wind turbines." Geomech. Energy Environ. 10: 12–20. https://doi.org/10.1016/j.gete.2017.05.002.

Malvern, L. E. 1969. Introduction to the mechanics of a continuous medium. Upper Saddle River, NJ: Prentice Hall.

Merifield, R. S., S. W. Sloan, and H. S. Yu. 2001. "Stability of plate anchors in undrained clay." *Géotechnique* 51 (2): 141–153. https://doi.org/10.1680/geot.2001.51.2.141.

Murff, J., M. Randolph, S. Elkhatib, H. Kolk, R. Ruinen, P. Strom, and C. Thorne. 2005. "Vertically loaded plate anchors for deepwater applications." In *PInt. Symp. on Frontiers in Offshore Geotechnics*, 31–48. Boca Raton, FL: CRC Press.

Murff, J. D., and J. M. Hamilton. 1993. "P-ultimate for undrained analysis of laterally loaded piles." *J. Geotech. Eng.* 119 (1): 91–107. https://doi.org/10.1061/(ASCE)0733-9410(1993)119:1(91).

Musial, W., D. Heimiller, P. Beiter, G. Scott, and C. Draxl. 2016. 2016 offshore wind energy resource assessment for the United States. Golden, CO: NREL.

O'Loughlin, C., D. White, and S. Stanier. 2015. "Novel anchoring solutions for FLNG-opportunities driven by scale." In Vol. 6 of Offshore

- Technology Conf., 4314–4345. Houston: Offshore Technology Conference.
- O'Neill, M. P., M. F. Bransby, and M. F. Randolph. 2003. "Drag anchor fluke-soil interaction in clays." *Can. Geotech. J.* 40 (1): 78–94. https://doi.org/10.1139/t02-096.
- Potts, D. M., L. Zdravkovic, and L. Zdravković. 2001. Finite element analysis in geotechnical engineering: Application. London: Thomas Telford.
- Randolph, M. F., and G. T. Houlsby. 1984. "The limiting pressure on a circular pile loaded laterally in cohesive soil." *Géotechnique* 34 (4): 613–623. https://doi.org/10.1680/geot.1984.34.4.613.
- Ranjan, G., and V. Arora. 1980. "Model studies on anchors under horizontal pull in clay." In *Proc., 3rd Australia-New Zealand Conf. on Geomechanics*, 65–70. Wellington, New Zealand: Institution of Professional Engineers New Zealand.
- Rowe, R. K., and E. H. Davis. 1982. "The behaviour of anchor plates in clay." *Géotechnique* 32 (1): 9–23. https://doi.org/10.1680/geot.1982.32.1.9.

- SIMULIA. 2018. ABAQUS/standard user's manual, version 2018. Providence, RI: SIMULIA.
- Song, Z., Y. Hu, D. Wang, and C. O'Loughlin. 2006. "Pullout capacity and rotational behaviour of square anchors." In *Proc.*, 6th Int. Conf. on Physical Modelling in Geotechnics, 1325–1331. London: Taylor & Francis.
- Wang, D., B. Bienen, M. Nazem, Y. Tian, J. Zheng, T. Pucker, and M. F. Randolph. 2015. "Large deformation finite element analyses in geotechnical engineering." *Comput. Geotech.* 65: 104–114. https://doi.org/10.1016/j.compgeo.2014.12.005.
- Yang, M., J. D. Murff, and C. P. Aubeny. 2010. "Undrained capacity of plate anchors under general loading." J. Geotech. Geoenviron. Eng. 136 (10): 1383–1393. https://doi.org/10.1061/(ASCE)GT .1943-5606.0000343.
- Yu, L., J. Liu, X.-J. Kong, and Y. Hu. 2011. "Numerical study on plate anchor stability in clay." *Géotechnique* 61 (3): 235–246. https://doi.org/10.1680/geot.8.P.071.